An adaptive central-upwind weighted essentially non-oscillatory scheme

X.Y. Hu [a,*], Q. Wang [a,b], N.A. Adams [a]

[a] *Lehrstuhl für Aerodynamik, Technische Universität München, 85748 Garching, Germany*
[b] *Chinese Academy of Aerospace Aerodynamics, 100074 Beijing, China*

ARTICLE INFO

ABSTRACT

In this work, an adaptive central-upwind 6th-order weighted essentially non-oscillatory (WENO) scheme is developed. The scheme adapts between central and upwind schemes smoothly by a new weighting relation based on blending the smoothness indicators of the optimal higher order stencil and the lower order upwind stencils. The scheme achieves 6th-order accuracy in smooth regions of the solution by introducing a new reference smoothness indicator. A number of numerical examples suggest that the present scheme, while preserving the good shock-capturing properties of the classical WENO schemes, achieves very small numerical dissipation.

© 2010 Elsevier Inc. All rights reserved.

1. Introduction

High-order weighted essentially non-oscillatory (WENO) schemes [8,3] are discretization schemes which are generally suitable for the simulation of shock-turbulence interaction due to their high-resolution properties. WENO schemes use a dynamic set of upwind stencils, where a nonlinear convex combination of lower order approximation polynomials adapts either to a higher order approximation in smooth regions of the solution, or to a lower-order spatial discretization that avoids interpolation across discontinuities and provides the necessary numerical dissipation for shock capturing. The weights of the convex combination are based on local smoothness indicators. The basic weighting strategy is to assign small weights to those lower order polynomials whose underlying stencils contain discontinuities, so that an essentially non-oscillatory solution is obtained. For smooth regions of the solution, optimal weights are used for each of the lower-order polynomials to achieve in combination an upwind scheme of maximum order. However, it is known that, while reproducing sharp shock profiles, the WENO scheme is still much more dissipative than central schemes, particularly in regions without strong shock wave but with large density variation or shear rates.

Generally, there are two approaches to decrease excessive dissipation of a WENO scheme. One approach is to resort to hybrid methods, where a low-dissipation scheme is switched on or off depending on indicators reflecting the flow-field properties [2,14,15,11]. Besides of increasing the complexity of the overall discretization scheme, the choice of an effective discontinuity detector remains a problematic issue for these methods when applied to complex applications. Additionally, some hybrid schemes, such as a hybrid of a high-order linear scheme and a robust non-linear shock-capturing scheme, can possibly cause numerical instabilities when multiple discontinuities are closely located, i.e. separated by only very few grid points [10]. An alternative approach is to modify the weighting strategy within the WENO methodology to achieve less numerical dissipation in smooth and moderate flow regions. As no other scheme or specific discontinuity detector is used, this approach is easy to implement and more suitable for complex applications. Approaches of this type can achieve less numerical dissipation than the classical WENO scheme, however, currently, they are still considerably more dissipative than hybrid schemes.

---

* Corresponding author.
  E-mail address: Xiangyu.Hu@aer.mw.tum.de (X.Y. Hu).

Up to now, two different improved weighting strategies have been developed for reducing numerical dissipation. One weighting strategy is to increase the bias towards the maximum-order upwind scheme in smooth regions. With the WENO-M scheme [7], WENO weights are pushed smoothly to the optimal values by a regularization process. With a slightly different weighting formulation, the WENO-Z scheme [4] normalizes the smoothness indicators by a reference value which drives the WENO weights to the optimal values faster than the classical WENO scheme. In the WENO-RL or WENO-RLTV scheme [20], the optimal weights are switched on directly when the maximum relative ratio between the smoothness indicators is of order $\mathcal{O}(10)$. While the WENO-M and WENO-Z schemes still have good shock-capturing properties, it is not clear whether the WENO-RL or WENO-RLTV maintain those properties when there are strong shocks or expansion waves. Another weighting strategy is to use the optimal weight for the central, other than upwind, scheme of maximum order by including the contribution of the downwind stencil. In WENO-SYMOO and WENO-SYMBO schemes [13], the optimal central scheme is used for better bandwidth efficiency. However, while the order of WENO-SYMBO scheme in smooth regions of the solution degenerates, the WENO-SYMOO scheme introduces numerical instabilities near the contact surfaces even when only moderately strong shock waves are involved. Furthermore, it is not clear whether the WENO-SYMOO scheme can achieve optimal order in smooth regions of the solution.

In this paper, we propose an adaptive central-upwind 6th-order WENO scheme. While the new scheme recovers the 6th-order central scheme with optimal weights, it adapts between the central and upwind schemes smoothly by a new weighting strategy based on the smoothness indicators of the optimal higher order stencil and lower order upwind stencils, and achieves 6th-order accuracy formally in smooth regions of the solution. The numerical examples show that the present scheme maintains the good shock-capturing properties of the classical WENO scheme and can achieve very small numerical dissipation.

2. Method

2.1. Weighted essentially non-oscillatory (WENO) scheme

For completeness, we briefly describe the classical 5th-order WENO scheme [8] in the context of the one-dimensional advection equation

$$\frac{\partial u}{\partial t} + \frac{\partial}{\partial x} f(u) = 0, \tag{1}$$

with positive advection speed, i.e. $\frac{df}{du} > 0$. Eq. (1) is discretized in the spatial domain such that $x_i = i\Delta x$, $i = 0,\ldots,N$, where Δx is the cell size, and $u_i = u(x_i)$. The semi-discretized form of Eq. (1) by the method of lines yields a system of ordinary differential equations

$$\frac{du_i}{dt} = -\frac{\partial f}{\partial x}\bigg|_{x=x_i}, \quad i = 0,\ldots,N. \tag{2}$$

Once the right-hand side of this expression has been evaluated, TVD Runge–Kutta methods are employed to advance the solution in time. A conservative finite difference formulation requires high-order consistent numerical fluxes at the cell faces. The conservative property of the spatial discretization is obtained by reconstructing the primitive function $h(x)$ implicitly as

$$f(x) = \frac{1}{\Delta x} \int_{x-\Delta x/2}^{x+\Delta x/2} h(\xi) d\xi, \tag{3}$$

such that the spatial derivative in Eq. (3) is approximated exactly by a conservative finite difference formula at the cell faces,

$$\frac{du_i}{dt} = -\frac{1}{\Delta x}(h_{i+1/2} - h_{i-1/2}). \tag{4}$$

In practice, Eq. (4) is approximated as

$$\frac{du_i}{dt} \approx -\frac{1}{\Delta x}(\hat{f}_{i+1/2} - \hat{f}_{i-1/2}), \tag{5}$$

where $\hat{f}_{i\pm1/2}$, reconstructed from known cell average values f_i, are approximations of $h_{i\pm1/2}$. As shown in Fig. 1, $\hat{f}_{i+1/2}$ is built by a convex combination of three candidate numerical fluxes $\hat{f}_{k,i+1/2}$ calculated from upwind 3-point stencils, i.e. S_0, S_1 and S_2.

$$\hat{f}_{i+1/2} = \sum_{k=0}^{2} \omega_k \hat{f}_{k,i+1/2}. \tag{6}$$

To obtain $\hat{f}_{k,i+1/2}$, 2nd-degree polynomial approximations are postulated

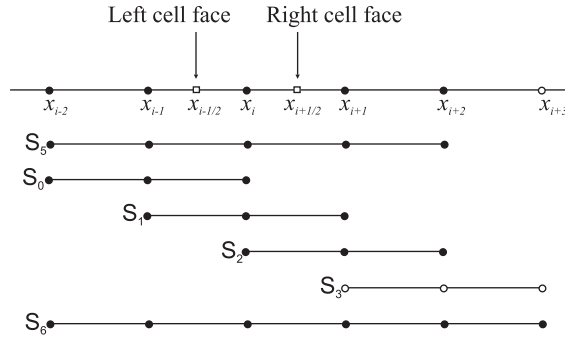$$h(x) \approx \hat{f}_k(x) = a_{0,k} + a_{1,k}x + a_{2,k}x^2, \tag{7}$$

Fig. 1. The computational uniform grid x_i: the 5-point stencil S_5 composed of three 3-points stencils S_0, S_1, S_2 and the 6-points stencil S_6 with an extra 3-point stencil S_3.

where $a_{0,k}$, $a_{1,k}$ and $a_{2,k}$ are found according to Eq. (3) and from the cell average values of the primitive function at the stencil nodes. Thus, for each stencil shown, a different 3rd-order approximation of the numerical flux function results. These approximations are evaluated at the cell face $i + 1/2$ and give the $\hat{f}_{k,i+1/2}$ of Eq. (6), i.e.

$$
\begin{aligned}
\hat{f}_{0,i+1/2} &= \frac{1}{6}(2f_{i-2} - 7f_{i-1} + 11f_i), \\
\hat{f}_{1,i+1/2} &= \frac{1}{6}(-f_{i-1} + 5f_i + 2f_{i+1}), \\
\hat{f}_{2,i+1/2} &= \frac{1}{6}(2f_i + 5f_{i+1} - f_{i+2}).
\end{aligned}
\tag{8}
$$

Since these linear combinations define the numerical flux at any cell face of the domain, an index-shift by -1 returns the corresponding $\hat{f}_{k,i-1/2}$. Taylor-series expansions of Eq. (8) result in

$$
\hat{f}_{k,i+1/2} = h_{i+1/2} + A_k \Delta x^3 + \mathcal{O}(\Delta x^4),
\tag{9}
$$

where A_k are independent of Δx. The weights ω_k in Eq. (6) are normalized by α_k, and defined as

$$
\omega_k = \frac{\alpha_k}{\sum_{k=0}^{2}\alpha_k}, \quad \alpha_k = \frac{d_k}{(\beta_k + \epsilon)^q}.
\tag{10}
$$

Here, $d_0 = \frac{1}{10}$, $d_1 = \frac{3}{5}$ and $d_2 = \frac{3}{10}$ are optimal weights since they generate the 5th-order upwind scheme, by which the numerical flux is computed from a 5-point stencil S_5, as shown in Fig. 1. $\epsilon > 0$ prevents division by zero and $q = 1$ or 2 is chosen to adjust the distinct weights at non-smooth parts of the solution. β_k are the smoothness indicators defined by

$$
\beta_k = \sum_{j=1}^{2} \Delta x^{2j-1} \int_{x_{i-1/2}}^{x_{i+1/2}} \left(\frac{d^j}{dx^j}\hat{f}_k(x)\right)^2 dx,
\tag{11}
$$

which have the discrete form

$$
\begin{aligned}
\beta_0 &= \frac{1}{4}(f_{i-2} - 4f_{i-1} + 3f_i)^2 + \frac{13}{12}(f_{i-2} - 2f_{i-1} + f_i)^2, \\
\beta_1 &= \frac{1}{4}(f_{i-1} - f_{i+1})^2 + \frac{13}{12}(f_{i-1} - 2f_i + f_{i+1})^2, \\
\beta_2 &= \frac{1}{4}(3f_i - 4f_{i+1} + f_{i+2})^2 + \frac{13}{12}(f_i - 2f_{i+1} + f_{i+2})^2.
\end{aligned}
\tag{12}
$$

Expansion of Eq. (12) as Taylor-series about f_i gives

$$
\begin{aligned}
\beta_0 &= f_i'^2 \Delta x^2 + \left(\frac{13}{12}f_i''^2 - \frac{2}{3}f_i'f_i'''\right)\Delta x^4 - \left(\frac{13}{6}f_i''f_i''' - \frac{1}{2}f_i'f_i^{(4)}\right)\Delta x^5 + \mathcal{O}(\Delta x^6), \\
\beta_1 &= f_i'^2 \Delta x^2 + \left(\frac{13}{12}f_i''^2 + \frac{1}{3}f_i'f_i'''\right)\Delta x^4 + \mathcal{O}(\Delta x^6), \\
\beta_2 &= f_i'^2 \Delta x^2 + \left(\frac{13}{12}f_i''^2 - \frac{2}{3}f_i'f_i'''\right)\Delta x^4 + \left(\frac{13}{6}f_i''f_i''' - \frac{1}{2}f_i'f_i^{(4)}\right)\Delta x^5 + \mathcal{O}(\Delta x^6).
\end{aligned}
\tag{13}
$$

The basic strategy of the weight definition Eq. (6) is that in smooth regions of the solution the smoothness indicators β_k are all small and have about the same magnitude, generating weights ω_k that approximate the optimal weights d_k. It can be found that a sufficient condition [7,4] for 5th-order accuracy of Eq. (5) is given by $\omega_k - d_k = \mathcal{O}(\Delta x^3)$. On the other hand, if

the stencil S_k contains a discontinuity, β_k is $\mathcal{O}(1)$ and the corresponding weight ω_k is small relative to the other weights. This implies that the contribution of the polynomial approximation of $h_{i\pm1/2}$ taken across the discontinuity is reduced, and the essentially non-oscillatory property is ensured by the convex combination of Eq. (6).

2.2. The optimal central scheme with 6-point stencil

Unlike the classical 5th-order WENO scheme, which uses the upwind scheme with a 5-point stencil, an alternative is to use the 6th-order interpolation with a 6-point stencil S_6, as shown in Fig. 1, as the scheme of maximum order with optimal weights [13]. The central scheme is derived by considering a 5th-degree polynomial approximation

$$h(x) \approx \hat{f}(x) = b_0 + b_1 x + b_2 x^2 + b_3 x^3 + b_4 x^4 + b_5 x^5, \tag{14}$$

with undetermined coefficients, b_k, where $k = 0,\ldots,5$. Substituting Eq. (14) into Eq. (3) and performing the integration gives

$$f(x) = b_0 + b_1 x + b_2 \left(x^2 + \frac{\Delta x^2}{12} \right) + b_3 \left(x^3 + \frac{x\Delta x^2}{12} \right) + b_4 \left(x^4 + \frac{x^2\Delta x^2}{2} + \frac{\Delta x^4}{80} \right) + b_5 \left(x^5 + \frac{5x^3\Delta x^2}{6} + \frac{x\Delta x^4}{16} \right). \tag{15}$$

The b_k are found by evaluating Eq. (15) at the stencil nodes, resulting in a system of six equations in the six unknown coefficients. Substituting these values of b_k into Eq. (14) and evaluating the numerical flux $\hat{f}_{i+1/2}$ gives

$$\hat{f}_{i+1/2} = \frac{1}{60} (f_{j-2} - 8f_{j-1} + 37f_j + 37f_{j+1} - 8f_{j+2} + f_{j+3}) = h_{i+1/2} + \frac{31}{4320} f_i^{(6)} \Delta x^6 + \mathcal{O}(\Delta x^7), \tag{16}$$

by Taylor-series expansion. To calculate the numerical flux $\hat{f}_{i-1/2}$, the stencil is shifted to the left by one grid spacing, and gives

$$\hat{f}_{i-1/2} = \frac{1}{60} (f_{j-3} - 8f_{j-2} + 37f_{j-1} + 37f_j - 8f_{j+1} + f_{j+2}) = h_{i-1/2} + \frac{31}{4320} f_i^{(6)} \Delta x^6 + \mathcal{O}(\Delta x^7), \tag{17}$$

by another Taylor-series expansion. Substitution of Eqs. (16) and (17) into Eq. (5) gives

$$\left. \frac{\partial f}{\partial x} \right|_{x=x_i} = \frac{1}{60} (-f_{j-3} + 9f_{j-2} - 45f_{j-1} + 45f_{j+1} - 9f_{j+2} + f_{j+3}) = f_i' + \mathcal{O}(\Delta x^6), \tag{18}$$

which is a 6th-order approximation of the derivative. As $\hat{f}_{i+1/2}$ and $\hat{f}_{i-1/2}$ are approximate with the same formulations, the lowest order truncation error terms are equal and cancel.

2.3. The downwind stencil and optimal weights

Following the methodology of the classical WENO scheme, a convex combination of $\hat{f}_{i+1/2}$, similarly as Eq. (6), is used to obtain $\hat{f}_{i+1/2}$ by

$$\hat{f}_{i+1/2} = \sum_{k=0}^{3} \omega_k \hat{f}_{k,i+1/2}. \tag{19}$$

However, an extra candidate stencil is included, i.e. the downwind stencil S_3 as shown in Fig. 1. S_3 gives an approximation

$$\hat{f}_{3,i+1/2} = \frac{1}{6} (11f_{i+1} - 7f_{i+2} + 2f_{i+3}), \tag{20}$$

whose Taylor-series expansion can be written in the form of in Eq. (9). In smooth regions of the solution, Eq. (19) recovers the 6th-order central scheme with 6-point stencil, and ω_k reduces to the optimal weights d_k. These weights can be determined as $d_0 = \frac{1}{20}$, $d_1 = \frac{9}{20}$, $d_2 = \frac{9}{20}$ and $d_3 = \frac{1}{20}$. Rewriting Eq. (19) by introducing optimal weights, including stencil S_3, gives

$$\hat{f}_{i+1/2} = \sum_{k=0}^{3} d_k \hat{f}_{k,i+1/2} + \sum_{k=0}^{3} (\omega_k - d_k) \hat{f}_{k,i+1/2}, \tag{21}$$

where the first term on the right-hand-side leads to a 6th-order approximation of the flux derivative as shown in Eq. (18). A sufficient condition for the approximation of Eq. (19) to be of 6th order is that the second term in Eq. (21) is at least $\mathcal{O}(\Delta x^7)$. Expanding this second term with Eq. (9) gives

$$\sum_{k=0}^{3} (\omega_k - d_k) \hat{f}_{k,i+1/2} = h_{i+1/2} \sum_{k=0}^{3} (\omega_k - d_k) + \Delta x^3 \sum_{k=0}^{3} A_k (\omega_k - d_k) + \sum_{k=0}^{3} (\omega_k - d_k) \mathcal{O}(\Delta x^4), \tag{22}$$

where the first term on the right-hand-side vanishes due to the normalization of the weights. Thus, it is sufficient to require that

$$\omega_k - d_k = \mathcal{O}(\Delta x^4), \tag{23}$$

for the overall scheme to retain 6th-order accuracy. Note that, this condition may be relaxed further by considering possible cancellation effects when the derivative is calculated with the same stencils for $\hat{f}_{i+1/2}$ and $\hat{f}_{i-1/2}$ [7,4].

2.4. The non-oscillatory weights

Inspired by Borges et al. [4], in this paper, the WENO weights are given by

$$\omega_k = \frac{\alpha_k}{\sum_{k=0}^{3}\alpha_k}, \quad \alpha_k = d_k\left(C + \frac{\tau_6}{\beta_k + \epsilon}\right), \tag{24}$$

where $\epsilon = 10^{-40}$, $k = 0, 1, 2$ and 3, which now includes, however, the contribution of the downwind stencil S_3. While Eq. (24) has a similar form as the WENO-Z scheme of Borges et al. [4], a new parameter $C \gg 1$ is introduced to increase the contribution of optimal weights when the smoothness indicators have comparable magnitudes [20]. Also a new reference smoothness indicator τ_6 is used. β_k, $k = 0, 1, 2$, are the smoothness indicators defined in Eq. (12). For β_3 the smoothness indicator of S_3 is not used but replaced by that of the 6-point stencil for the 6th-order interpolation, which is calculated by Eqs. (11) and (14), i.e.

$$\begin{aligned}
\beta_3 = \beta_6 = \frac{1}{10080}&\Big[271779f_{j-2}^2 + f_{j-2}(2380800f_{j-1} + 4086352f_j - 3462252f_{j+1} + 1458762f_{j+2} - 245620f_{j+3}) \\
&+ f_{j-1}(5653317f_{j-1} - 20427884f_j + 17905032f_{j+1} - 7727988f_{j+2} + 1325006f_{j+3}) + f_j(19510972f_j \\
&- 35817664f_{j+1} + 15929912f_{j+2} - 2792660f_{j+3}) + f_{j+1}(17195652f_{j+1} - 15880404f_{j+2} + 2863984f_{j+3}) \\
&+ f_{j+2}(3824847f_{j+2} - 1429976f_{j+3}) + 139633f_{j+3}^2\Big].
\end{aligned} \tag{25}$$

Eq. (24) implies three different weighting relations: the first is between the upwind stencils and the downwind stencil; the second is within the different upwind stencils; the third involves all the stencils. The first weighting relation compares the values of $\frac{\tau_6}{\beta_3 + \epsilon}$ and $\frac{\tau_6}{\beta_k + \epsilon}$ for $k = 0, 1, 2$, and identifies the smoothness of a local flow field. If it is sufficiently smooth the optimal central scheme is used. Otherwise, the contribution of the downwind stencil vanishes and the dominant stencil is determined by comparing the values of $\frac{\tau_6}{\beta_k + \epsilon}$ for $k = 0, 1, 2$ (the second weighting relation, which corresponds to the classical WENO scheme). Furthermore, when all smoothness indicators have comparable magnitudes, the third weighting relation pushes the weights towards their optimal values due to the large value of C.

The reference smoothness indicator τ_6 is defined by

$$\tau_6 = \beta_6 - \frac{1}{6}(\beta_0 + \beta_2 + 4\beta_1). \tag{26}$$

With Taylor-series expansions, Eqs. (12) and (25) imply that

$$\begin{aligned}
\beta_6 &= f_i'^2\Delta x^2 + \frac{13}{12}f_i''^2\Delta x^4 + \mathcal{O}(\Delta x^6), \\
\frac{1}{6}(\beta_0 + \beta_2 + 4\beta_1) &= f_i'^2\Delta x^2 + \frac{13}{12}f_i''^2\Delta x^4 + \mathcal{O}(\Delta x^6),
\end{aligned} \tag{27}$$

so that τ_6 is of order $\mathcal{O}(\Delta x^6)$. Note that τ_6 is different from τ_5 in Yamaleev and Carpenter [22], where it is found that a direct application of τ_5 (the WENO-NW scheme) leads to numerical instability and needs extra dissipation (the ESWENO scheme). As shown by Yamaleev and Carpenter [22], τ_5 is basically the 5th-degree undivided difference on the 6-point stencil and proportional to the highest-order component of β_6 [16]. With Eqs. (12) and (27), one can find that

$$\frac{\tau_6}{\beta_k + \epsilon} = \mathcal{O}(\Delta x^4), \quad k = 0, 1, 2, 3, \tag{28}$$

which indicates that, independent of the value of C, Eq. (24) satisfies the condition of Eq. (23) for 6th-order accuracy in smooth regions of the solution. Note that Eq. (28) is not valid when critical points or discontinuities are present. In the first case, similarly to classical WENO5, the accuracy or approximation degenerates since β_k decreases to the order of $\mathcal{O}(\Delta x^4)$ and the condition of Eq. (23) cannot be satisfied. Although limited success on resolving critical points has been achieved by modifying Eq. (24) as in Borges et al. [4], we prefer not to use such a modification since, as also pointed out by Borges et al. [4], it increases numerical dissipation considerably. In the second case, one has $\beta_6 \gg \beta_k$ and $\alpha_k \gg \alpha_3$, $k = 0, 1, 2$, by which the weight for $\hat{f}_{3,i+1/2}$ calculated from the downwind stencil S_3 vanishes. The dominant weight will be assigned to one of $\hat{f}_{k,i+1/2}$ calculated from the upwind stencil with the minimum value of the smoothness indicator.

3. Numerical examples

The following numerical examples are provided to illustrate the potential of the proposed adaptive central-upwind WENO scheme. For the linear advection problem, the one-dimensional linear advection equation

$$\frac{\partial u}{\partial t} + \frac{\partial u}{\partial x} = 0, \tag{29}$$

is used. For other problems, the flow is described by the compressible Euler equations

$$\begin{pmatrix} \rho \\ \rho u \\ \rho v \\ \rho w \\ E \end{pmatrix}_t + \begin{pmatrix} \rho u \\ \rho u^2 + p \\ \rho u v \\ \rho u w \\ (E+p)u \end{pmatrix}_x + \begin{pmatrix} \rho v \\ \rho v u \\ \rho v^2 + p \\ \rho v w \\ (E+p)v \end{pmatrix}_y + \begin{pmatrix} \rho w \\ \rho w u \\ \rho w v \\ \rho w^2 + p \\ (E+p)w \end{pmatrix}_z = 0. \tag{30}$$

This set of equations describes the conservation laws expressed by mass density ρ, momentum density $\rho\mathbf{v} \equiv (\rho u, \rho v, \rho w)$ and total energy density $E = \rho e + \frac{1}{2}\rho\mathbf{v}^2$, where e is the internal energy per unit mass. To close this set of equations, the ideal-gas equation of state $p = (\gamma - 1)\rho e$ with $\gamma = 1.4$ is used.

These equations are solved by following the general WENO methodology [8] except that the interpolation is applied with the proposed adaptive central-upwind WENO scheme, which is denoted as WENO-CU6. Specifically, the Roe approximation is used for the characteristic decomposition at the cell faces, the Lax-Friedrichs formulation is used for the numerical fluxes, and the 3rd-order TVD Runge–Kutta scheme is used for time integration (Shu and Osher, 1988). Following the choice of Taylor et al. [20], the constant C in Eq. (24) should be of order $\mathcal{O}(10)$. We set $C = 20$ for all numerical examples (see also a study of the sensitivity of C in Section 3.4). If not mentioned otherwise, for one-dimensional examples, the number of grid points is 200 and the exact solution, if given, is sampled on 200 grid points. All the computations are carried out with a CFL number of 0.6.

3.1. Linear advection problem

First, we verify that the WENO-CU6 scheme recovers the theoretical order of convergence for smooth solutions. We consider a one-dimensional linear advection problem from Yamaleev and Carpenter [22], described by Eq. (29) with initial condition

$$u = e^{-300(x-x_c)^2},$$

where $x_c = 0.5$. A periodic boundary condition is applied at $x = 0$ and $x = 1$. The final time is $t = 1$, which corresponds to one period. For the convergence study, this problem is computed on different grids with $N = 51, 101, 201, 401, 801$ and 1601 grid points. The peak of the Gaussian pulse propagates to the middle grid point at $t = 1$. The time-step sizes are decreased until the effect of the temporal truncation error is negligible. Fig. 2 gives the error distributions and convergence of the L_∞ error. The WENO-CU6 scheme achieves the theoretical order of accuracy. We observe that the maximum error does not occur at the peak value of the exact solution (see Fig. 2(a)), unlike for the 6th-order ESWENO scheme of Yamaleev and Carpenter [22].

3.2. Shock-tube problems

Here, we show that the proposed scheme WENO-CU6 passes the shock-tube test problems: the Sod problem [19], the Lax problem [12] and the 123 problem [5]. For the Sod problem, the initial condition is

$$(\rho, u, p) = \begin{cases} (1, 0, 1) & \text{if } 0 < x < 0.5, \\ (0.125, 0, 0.1) & \text{if } 1 > x > 0.5, \end{cases}$$
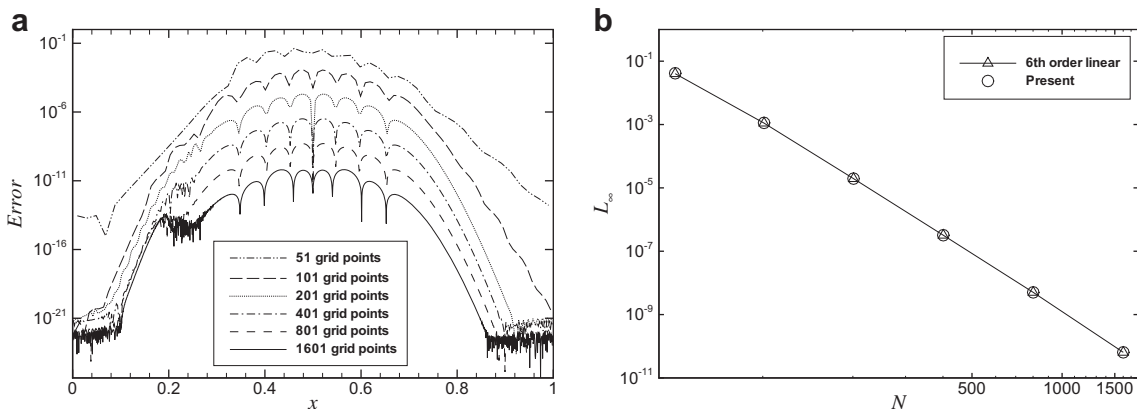

Fig. 2. Linear advection problem at $t = 1$: (a) Error distribution; (b) Convergence of the L_∞ error.

and the final time is $t = 0.2$. For the Lax problem, the initial condition is

$$(\rho, u, p) = \begin{cases} (0.445, 0.698, 0.3528) & \text{if } 0 < x < 0.5, \\ (0.5, 0, 0.5710) & \text{if } 1 > x > 0.5, \end{cases}$$

and the final time is $t = 0.14$. For the 123 problem, the initial condition is

$$(\rho, u, p) = \begin{cases} (1, -2, 0.4) & \text{if } 0 < x < 0.5, \\ (1, 2, 0.4) & \text{if } 1 > x > 0.5, \end{cases}$$

and the final time is $t = 0.1$. Fig. 3 gives the computed velocity and density distributions, which show good agreement with the exact solutions. While providing good shock-capturing properties, the WENO-CU6 produces less numerical dissipation than the classical 5th-order WENO, WENO-M schemes, especially near the discontinuities (see Fig. 12 in Henrick et al. [7]). Note that, although the downwind stencil is included, the WENO-CU6 does not experience numerical instability near the discontinuity as shown by Martin (2006) (their Fig. 9) for their WENO-SYMOO scheme and by Yamaleev and Carpenter (2009) (their Fig. 9) for their WENO-NW scheme. This can be expected since, when there is a discontinuity, the weight for the downwind stencil becomes much smaller than those for the upwind stencils as implied by the smoothness indicator for the 6th-order stencil of the central scheme in Eq. (26). Due to very small numerical dissipation, slight velocity overshoots are produced near strong shock or expansion waves (see Figs. 3(a) and (c). These overshoots are numerical errors rather than
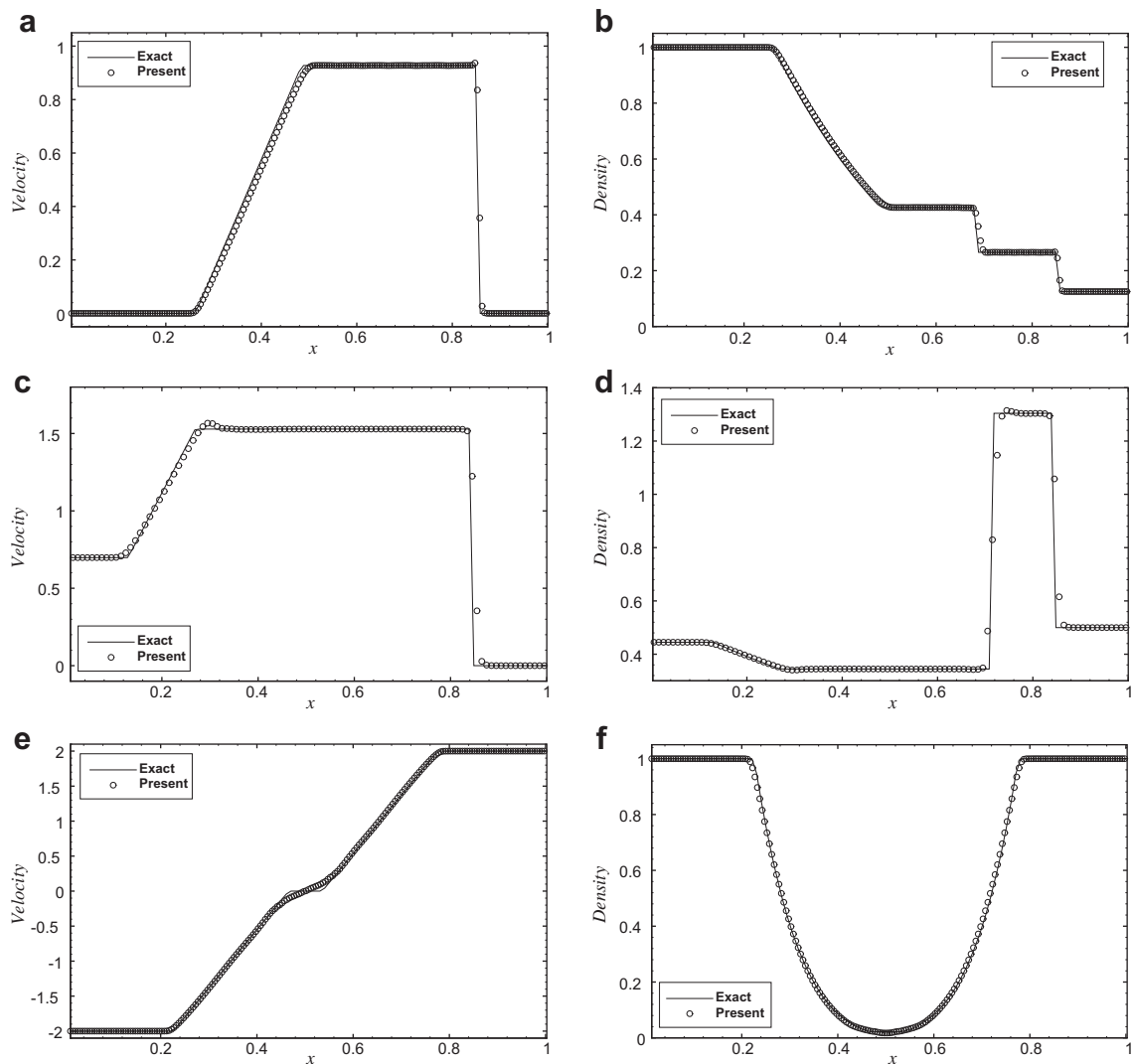

Fig. 3. Shock-tube problems: (a) Sod problem; (b) Lax problem (on a 100 points grid); (c) 123 problem.

instabilities, since they do not propagate to other regions and their magnitudes decreases for increasing resolution (not shown here).

3.3. Interacting blast waves

We consider a two-blast-wave interaction problem, which is taken from Woodward and Colella [21]. The initial condition is

$$(\rho, u, p) = \begin{cases} (1, 0, 1000) & \text{if } 0 < x < 0.1, \\ (1, 0, 0.01) & \text{if } 0.1 < x < 0.9, \\ (1, 0, 100) & \text{if } 1 > x > 0.9, \end{cases}$$

and the final time is $t = 0.038$. The reflective boundary condition is applied at both $x = 0$ and $x = 1$. We examine the numerical solution on 400 and 800 grid points, and the reference "exact" solution is a high-resolution numerical solution on 3200 grid points calculated by the WENO-Z scheme [4]. Fig. 4(a) and (b) give the computed density profiles. Again, good agreement with the reference solutions is observed. Due to less numerical dissipation, the WENO-CU6 shows an improved solution, especially near the valley at about $x = 0.75$ and the right peak at about $x = 0.78$, compared to the results of classical 5th-order WENO, WENO-M and WENO-Z, (see Figs. 10 and 11 in Henrick et al. [7], and Fig. 9 in Borges et al. [4]). Note that, a slight overshoot of the density peak is produced in the low-resolution results (see the insert in Fig. 4(a)), and, again, this numerical error disappears for increasing resolution (see the insert in Fig. 4(b)).

3.4. Shock-density wave interaction

We consider a shock density-wave interaction problem [18]. The initial conditions are set by a Mach 3 shock interacting with a perturbed density field

$$(\rho, u, p) = \begin{cases} (3.857, 2.629, 10.333) & \text{if } 0 \leqslant x < 1 \\ (1 + 0.2\sin(5x), 0, 1) & \text{if } 10 \geqslant x > 1 \end{cases}$$

and the final time is $t = 1.8$. A zero-gradient boundary condition is applied at $x = 0$ and 10. Fig. 5(a) and (b) show the calculated density and velocity profile at $t = 1.8$ with increasing number of points. We shall refer to the solution computed by the WENO-Z scheme with 3200 grid points as the "exact" solution. As shown in Fig. 5(a), the WENO-CU6 gives a better resolved density waves behind the shock than the classical WENO scheme, the WENO-M scheme (see Figs. 8 and 9 in Henrick et al. [7]) and the WENO-SYMOO and WENO-SYMBO schemes (see Fig. 11 in Martin et al. [13]). Note that the WENO-CU6 is able to achieve a small numerical dissipation comparable to that of the hybrid method of Kim and Kwon [11] (see their Fig. 3) and the artificial nonlinear diffusivity method of Fiorina and Lele [6] (their Fig. 14). Note that more recent versions of artificial diffusivity methods achieve even less dissipation for this particular case, however, at the expense of spurious oscillations (see Fig. 18 in Kawai and Lele [10] and Fig. 3 in Johnsen et al. [9]).

Fig. 6 gives the density and velocity profiles on 200 grid points with two different values of the constant C in Eq. (24). It can be found that, increasing or decreasing the value of C within the order $\mathcal{O}(10)$ range only changes the numerical dissipation slightly. However, since excessively large values of C may lead to numerical instabilities for problems with strong shock waves, such as for interacting blast waves, a moderate value $C = 20$ is used for all numerical examples in this paper.
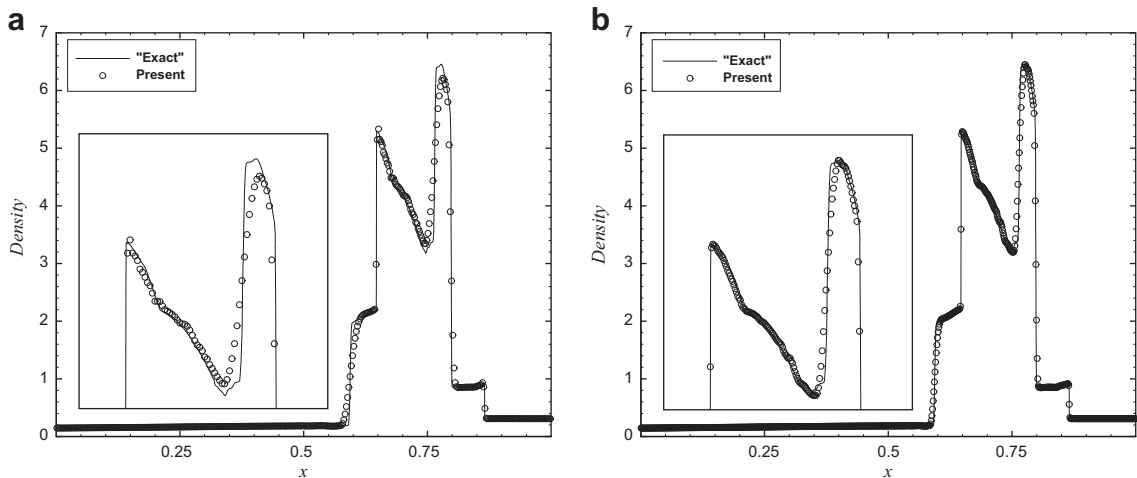

Fig. 4. Interacting blast waves: (a) density profile on a 400 points grid; (b) density profile on a 800 points grid.
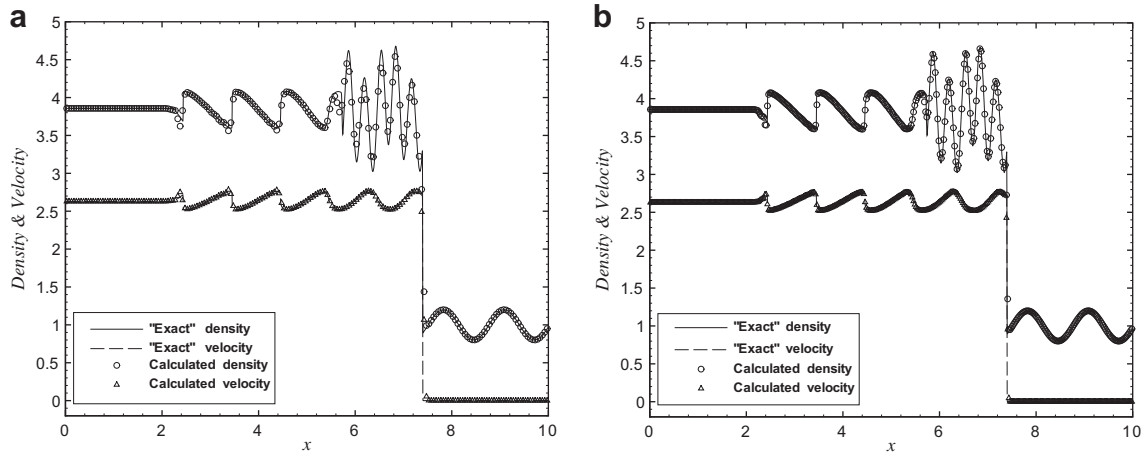
Fig. 5. Shock-density-wave interaction: (a) density and velocity profiles on a 200 points grid; (b) density and velocity profiles on a 400 points grid.
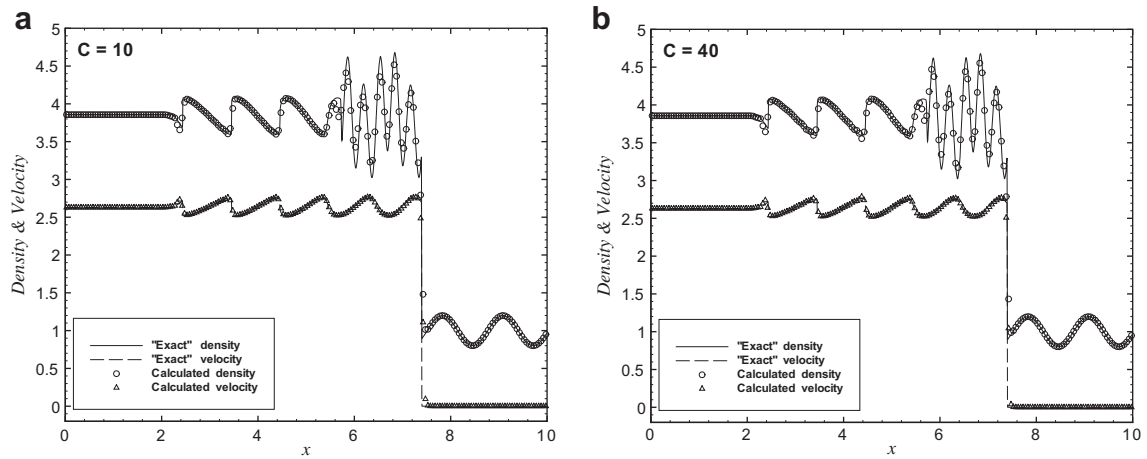

Fig. 6. Shock-density-wave interaction with influence of constant C in Eq. (24): (a) C = 10; (b) C = 40.

3.5. Advection of an isentropic vortex

We consider a problem from Yee et al. [23], where an isentropic vortex is convected an inviscid free stream. The computations are performed on the flow domain of $[0,0] \times [10,10]$. An isentropic vortex is added to the mean flow, and the initial flow field is given by

$$\rho = \left[1 - \frac{(\gamma - 1)\beta^2}{8\gamma\pi^2} e^{(1-r^2)} \right]^{\frac{1}{\gamma-1}}, \quad r^2 = \bar{x}^2 + \bar{y}^2,$$

$$(u, v) = (1, 1) + \frac{\beta}{2\pi} e^{\frac{1}{2}(1-r^2)}(-\bar{y}, \bar{x}), \quad \bar{x} = x - x_{vc}, \quad \bar{y} = y - y_{vc}$$

$$p = \rho^\gamma,$$

where $\beta = 5$, and $(x_{vc}, y_{vc}) = (5, 5)$ are the coordinates of the center of initial vortex. The final time is $t = 10$, when the vortex has been convected along the diagonal of the computational domain and arrives at the initial location. Periodic boundary conditions are implemented in both directions. Note that, although the flow is smooth over the entire domain, there are critical points at the center of the vortex and symmetric planes.

Fig. 7 shows the calculated density and velocity component u profiles on a 50×50 grid. It can be found that there is no visible difference between the computed results at $t = 10$ and the initial profile. For a convergence test, this problem is simulated using various grid: 25×25, 50×50, 75×75 and 100×100. The resulting error and convergence rates are shown in Table 1. Compared to the results of the hybrid method of Kim and Kwon [11], the WENO-CU6 produces considerably smaller L_1 and L_∞ errors and higher overall convergence rate. Note that the accuracy of present results on a 75×75 grid is already higher than that on a 100×100 grid gives Kim and Kwon [11] (see their Table 2).
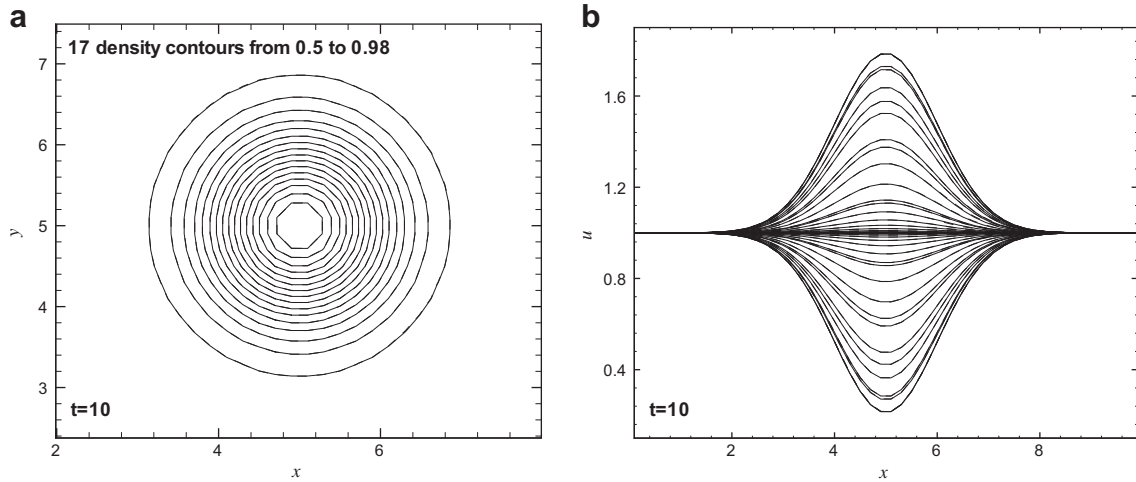
Fig. 7. Advection of an isentropic vortex at t = 10, calculated on a 50 × 50 grid: (a) density contours (theory: solid, calculated: dashed); (b) profile of velocity component u along x axis (theory: solid, calculated: dashed).

Table 1
Convergence test for the vortex evolution problem.

Resolution	L_1 error	L_1 order	L_∞ error	L_∞ order
25 × 25	1.82328×10^{-3}	–	3.65921×10^{-2}	–
50 × 50	6.50249×10^{-5}	4.81	1.07542×10^{-3}	5.09
75 × 75	7.07898×10^{-6}	5.47	1.49496×10^{-4}	4.87
100 × 100	1.82747×10^{-6}	5.15	4.11929×10^{-5}	4.70

3.6. Shock wave interacting with fluctuations

We consider the problem from Shu and Osher [18] on the interaction between shock wave and velocity fluctuations. A Mach 8 shock in air moves into an oblique divergence free vorticity fluctuation field. For this case, the initial condition is

$$(\rho, u, v, p) = \begin{cases} (1, u_r, v_r, 1) & \text{if } x > 0.5 \\ (5.565, 7.765, 0, 74.5) & \text{else} \end{cases}$$

and the final time is t = 0.2. Here, the fluctuating velocity field is given by

$$u_r = -c_r \sin\theta \cos[(x - 1.5)k\cos\theta + (y - 1)k\sin\theta],$$
$$v_r = c_r \sin\theta \cos[(x - 1.5)k\cos\theta + (y - 1)k\sin\theta],$$

where $c_r = \sqrt{\gamma}$ is the pre-shock sound speed. The computational domain of this problem is $[0,0] \times [4,2]$. Periodic boundary conditions in are implemented at the top and bottom of the domain. An inflow boundary is applied at the left end of the domain. Since the disturbance from the right end of the domain does not reach the shock front within the computing time, simple zero-gradient extrapolation is implemented there.

Fig. 8 shows the pressure and vorticity contours of the solution with low-, medium- and high-resolution grids. It can be found that the high-resolution results, although with slightly larger grid sizes, are in good agreement with those calculated by the 3rd-order ENO scheme in Adams [1] (their Fig. 11). The results of low- and medium-resolutions are also in good agreement with those calculated by a 5-order hybrid scheme of Adams and Shariff [2]. Since the WENO-CU6 has higher order accuracy in smooth regions of the solution, it predicts a sharper vorticity gradient at the left fringe (see their Figs. 15(a) and 17(a)).

3.7. Double Mach reflection a strong shock

We consider the problem from Woodward and Colella [21] on the double Mach reflection of a strong shock. A Mach 10 shock in air is reflected from the wall with incident angle of 60^0. For this case, the initial condition is

$$(\rho, u, v, p) = \begin{cases} (1.4, 0, 0, 1) & \text{if } y < 1.732(x - 0.1667), \\ (8, 7.145, -4.125, 116.8333) & \text{else,} \end{cases}$$
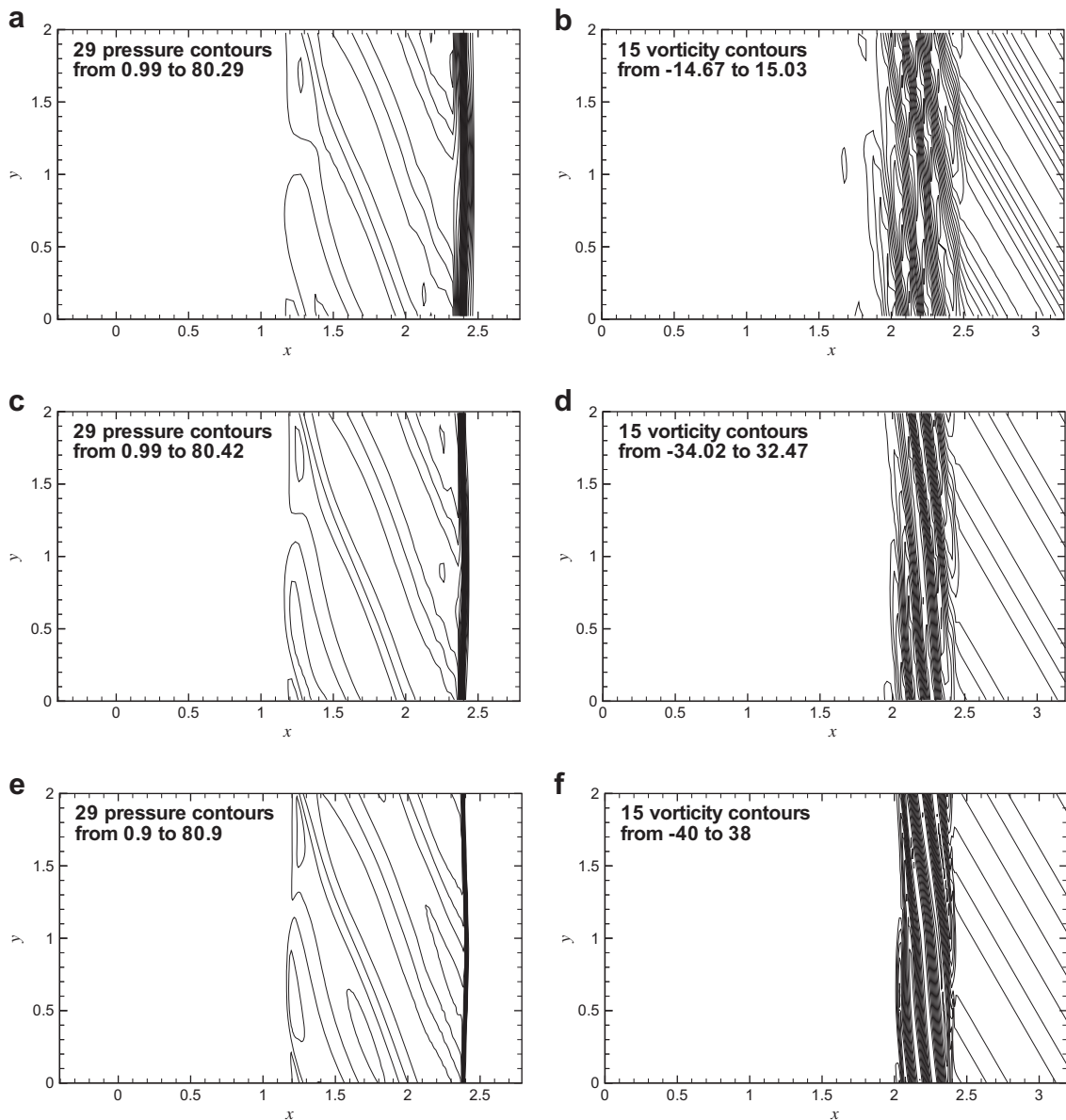
Fig. 8. Shock wave interacting with fluctuations at $t = 0.2$: (left) pressure contours, (right) vorticity contours on a 80×40 grid ((a) and (b)), a 160×80 grid ((c) and (d)), and a 400×200 grid ((e) and (f)).

and the final time is $t = 0.2$. The computational domain of this problem is $[0,0] \times [4,1]$. Initially, the shock extends from the point $x = 0.1667$ at the bottom to the top of the computational domain. Along the bottom boundary, at $y = 0$, the region from $x = 0$ to $x = 0.1667$ is always assigned post-shock conditions, whereas a reflecting wall condition is set from $x = 0.1667$ to $x = 4$. Inflow and outflow boundary conditions are applied at the left and right ends of the domain, respectively. The values at the top boundary are set to describe the exact motion of a Mach 10 shock.

Fig. 9(a) shows the density contours of the solution on a 240×60 grid. Good agreement with the results at the same resolution in Fiorina and Lele [6] (their Fig. 21(b)) and in Kawai and Lele [10] (their Fig. 22(a)) is observed. Note that, while the WENO-CU6 predicts a slightly smeared slip-line, it resolves better the wave structures near the second triple point and predicts a stronger jet near the wall. Figs. 9(b) and (c) give the density contours of the solution on a 480×120 grid and a 960×240 grid. Again, a good agreement with the results at the same resolutions of Kim and Kwon [11] (their Figs. 12 and 13) and Kawai and Lele [10] (their Fig. 22(c)) is observed. As shown in a close-up view of the "blow-up" region (Fig. 10), the WENO-CU6 resolves considerably finer vortical structures and is less dissipative at small scales. The obtained results are comparable to that with twice the resolution computed by the classical 5th-order WENO scheme in Shu [17] (see their Fig. 11.7).
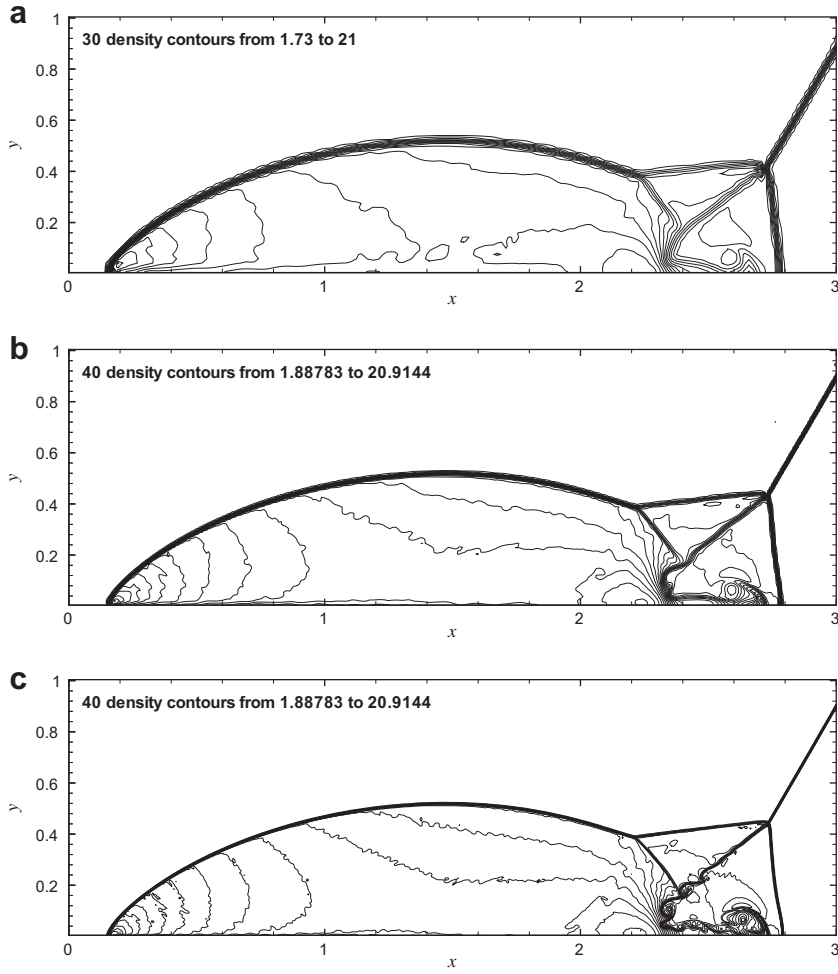
Fig. 9. Double-Mach reflection of a Mach 10 shock wave: density profile at $t = 0.2$, on (a) a 240 × 60 grid, (b) a 480 × 120 grid, and (c) a 960 × 240 grid.
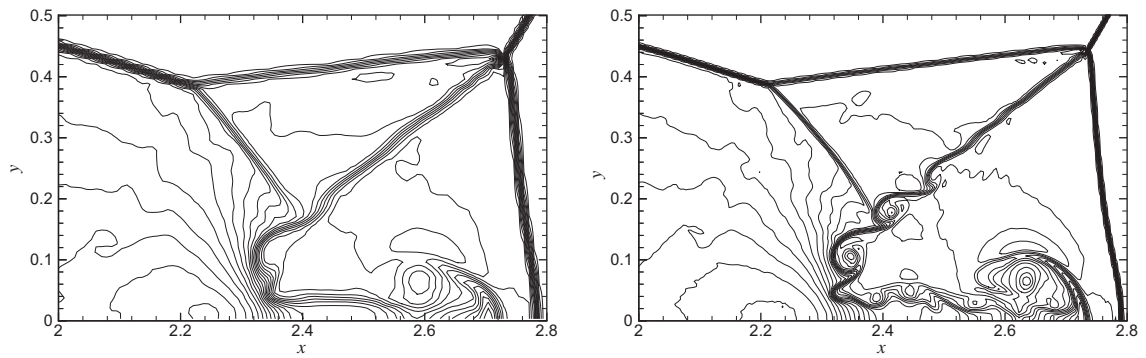

Fig. 10. Close-up view of the "blow-up" region of Fig. 9(b) (left) and (c) (right).

3.8. Nonlinear numerical dissipation

We consider a problem to study the nonlinear effective numerical dissipation of the WENO-CU6 scheme for a turbulence-like velocity spectrum. For the Euler equations an isotropic fluctuation field develops an equipartition spectrum for the kinetic energy. The effective numerical dissipation can be assessed by checking how much of the equipartition spectrum restored. Initially the flow field has constant density $\rho = 1$ and constant pressure $p = 100/\gamma$. The generated initial random
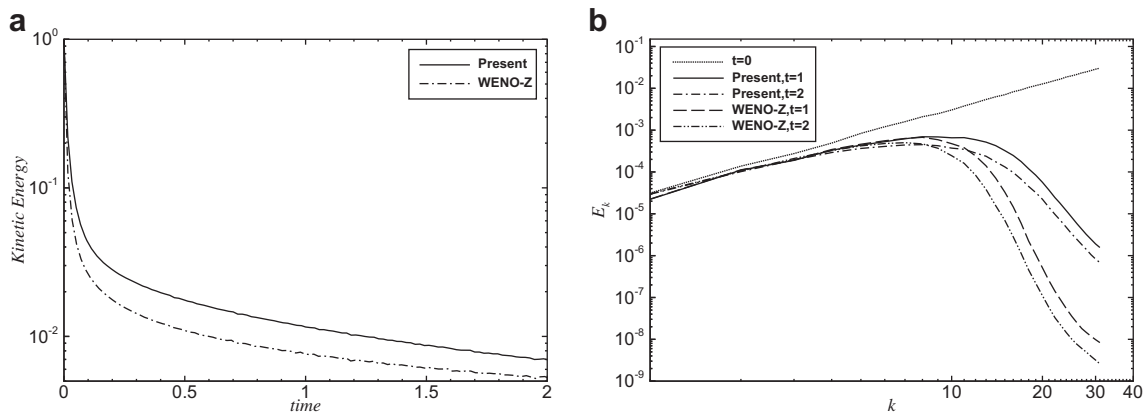
Fig. 11. Nonlinear numerical dissipation on a 64^3 grid: (a) temporal evolution of normalized mean kinetic energy, (b) energy spectra at $t = 0$, 1 and 2.

velocity field follows a Gaussian distribution function with zero mean and unit variance. The computations are performed on the flow domain of $[0,0,0] \times [2\pi, 2\pi, 2\pi]$ with 64^3 grid points. Periodic boundary conditions are implemented in all directions. The final time is $t = 2$.

Fig. 11 shows the temporal evolution of the mean kinetic energy normalized with its initial value and the energy spectra at $t = 0$, 1 and 2. As shown in Fig. 11(a), the kinetic energy decays very fast at the first several time steps. Note that the WENO-CU6 scheme preserves considerably more kinetic energy than the WENO-Z scheme. For example, after 10 time-steps, while the WENO-Z scheme preserves 13% of the initial kinetic energy, the WENO-CU6 scheme preserves about 23%. As shown in Fig. 11(b), the initial three dimensional energy spectrum $E_k \propto k^2$, where k is wave number, should be preserved for an exact solution of the Euler equations. Since the numerical dissipation increases with wave number, the later-time energy spectra increasingly deviate from the initial profile for increasing wave numbers. Furthermore, there is no pile-up of kinetic energy at large wave numbers owing to the shock-capturing property of WENO schemes. Note that, compared to the WENO-Z scheme, the WENO-CU6 has much less numerical dissipation at large wave numbers and therefore preserves much more small-scale dynamics.

4. Concluding remarks

In this paper, we have proposed an adaptive central-upwind 6th-order WENO scheme. It adapts between central and upwind schemes smoothly by a weighting strategy based on the operations between the smoothness indicators of the optimal higher order stencil and lower order upwind stencils, and achieves 6th-order accuracy in smooth regions of the solution by introducing a new reference smoothness indicator. There is a parameter of order $\mathcal{O}(10)$ associated with the relative smoothness as in Taylor et al. [20]. However, the numerical dissipation is not sensitive to the parameter, and a fixed value is broadly effective without tuning. The results of the numerical examples suggest that the present scheme is suitable for direct numerical simulation of interactions between turbulent flows and shock waves because of low numerical dissipation and good shock-capturing properties.

References

[1] N.A. Adams, The use of LES subgrid-scale models for shock capturing, Int. J. Numer. Meth. Fluids 39 (2002) 783–797.
[2] N.A. Adams, K. Shariff, A high-resolution hybrid compact-ENO scheme for shock-turbulence interaction problems, J. Comput. Phys. 127 (1996) 27–51.
[3] D. Balsara, C.W. Shu, Monotonicity preserving weighted essentially non-oscillatory schemes with increasingly high order accuracy, J. Comput. Phys. 160 (2000) 405–452.
[4] R. Borges, M. Carmona, B. Costa, W.S. Don, An improved weighted essentially non-oscillatory scheme for hyperbolic conservation laws, J. Comput. Phys. 227 (2008) 3191–3211.
[5] B. Einfeldt, C.D. Munz, P.L. Roe, B. Sjögreen, On Godunov-type methods near low densities, J. Comput. Phys. 92 (1991) 273–295.
[6] B. Fiorina, S.K. Lele, An artificial nonlinear diffusivity method for supersonic reacting flows with shocks, J. Comput. Phys. 222 (2007) 246–264.
[7] A.k. Henrick, T.D. Aslam, J.M. Powers, Mapped weighted essentially non-oscillatory schemes: achieving optimal order near critical points, J. Comput. Phys. 207 (2005) 542–567.
[8] G.S. Jiang, C.W. Shu, Efficient implementation of weighted ENO schemes, J. Comput. Phys. 126 (1996) 202–228.
[9] E. Johnsen, J. Larsson, A.V. Bhagatwala, W.H. Cabot, P. Moin, B.J. Olson, P.S. Rawat, S.K. Shankar, B. Sjögreen, H.C. Yee, X.L. Zhong, S.K. Lele, Assessment of high-resolution methods for numerical simulations of compressible turbulence with shock waves, J. Comput. Phys. 229 (2010) 1213–1237.
[10] S. Kawai, S.K. Lele, Localized artificial diffusivity scheme for discontinuity capturing on curvilinear meshes, J. Comput. Phys. 227 (2008) 9498–9526.
[11] D. Kim, H.K. Kwon, A high-order accurate hybrid scheme using a central flux scheme and a WENO scheme for compressible flowfield analysis, J. Comput. Phys. 210 (2005) 554–583.
[12] P.D. Lax, Weak solution of non-linear hyperbolic equations and their numerical computations, Commun. Pure Appl. Math. 7 (1954) 159–193.
[13] M.P. Martin, E.M. Taylor, M. Wu, V.G. Weirs, A bandwidth-optimized WENO scheme for the effective direct numerical simulation of compressible turbulence, J. Comput. Phys. 220 (2006) 270–289.
[14] S. Pirozzoli, Conservative hybrid compact-WENO schemes for shock-turbulence interaction, J. Comput. Phys. 178 (2002) 81–117.

[15] Y.X. Ren, M. Liu, H. Zhang, A characteristic-wise hybrid compact-WENO scheme for solving hyperbolic conservation laws, J. Comput. Phys. 192 (2003) 365–386.
[16] Y.Q. Shen, and G.C. Zha, A Robust seventh-order WENO Scheme and its applications. AIAA Paper 2008-0757, (2008).
[17] C.W. Shu, High Order ENO and WENO Schemes for Computational Fluid Dynamics, in: T.J. Barth, H. Deconinck (Eds.), High-order methods for computational physics, Springer, Berlin, 1999.
[18] C.W. Shu, S. Osher, Efficient implement of essentially non-oscillatory shock-wave schemes, II, J. Comput. Phys. 83 (1989) 32–78.
[19] G.A. Sod, A survey of several finite difference methods for systems of non-linear hyperbolic conservation laws, J. Comput. Phys. 27 (1978) 1–31.
[20] E.M. Taylor, M. Wu, M.P. Martin, Optimization of nonlinear error for weighted essentially non-oscillatory methods in direct numerical simulations of compressible turbulence, J. Comput. Phys. 223 (2007) 384–397.
[21] P. Woodward, P. Colella, The numerical simulation of two-dimensional fluid flow with strong shocks, J. Comput. Phys. 54 (1984) 115–173.
[22] N.K. Yamaleev, M.H. Carpenter, A systematic methodology for constructing high-order energy stable WENO schemes, J. Comput. Phys. 228 (2009) 4248–4272.
[23] H.C. Yee, N.D. Sandham, M.J. Djomehri, Low-dissipative high-order shock-capturing methods using characteristic-based filters, J. Comput. Phys. 150 (1999) 199–238.